



Discharge Precipitate's Impact in Li-Air Battery: Comparison of Experiment and Model Predictions

Yun Wang^{*,z} and Hao Yuan

Renewable Energy Resources Lab (RERL), Department of Mechanical and Aerospace Engineering, The University of California, Irvine, California 92697-3975, USA

This paper presents a fundamental study on the precipitate formation/morphology and impact of discharge precipitates in Li-air batteries and compares the voltage loss with two Li-air battery models, namely a film-resistor model and surface coverage model. Toray carbon cloth is selected as cathode, which serves as large-porosity electrodes with an approximately planar reaction surface. Imaging analysis shows film formation of precipitates is observed in all the experiments. In addition, toroidal and aggregate morphologies are present under lower currents as well. Specially, toroidal or partially toroidal deposit is observed for 0.06 A/cm². Aggregates, which consist of small particles with grain boundaries, are shown for 0.03 A/cm². We found that the film-resistor model is unable to predict the discharge voltage behaviors under the two lower currents due to the presence of the deposit morphologies other than the film formation. The coverage model's prediction shows acceptable agreement with the experimental data because the model accounts for impacts of various morphologies of precipitates.

© 2017 The Electrochemical Society. [DOI: 10.1149/2.0271712jes] All rights reserved.

Manuscript submitted May 1, 2017; revised manuscript received June 29, 2017. Published August 4, 2017.

Lithium-air (or Li-air) batteries hold a great promise for high specific energy storage. Its theoretical value can reach 3,505 Wh kg⁻¹ for non-aqueous electrolytes, which is closer to direct methanol fuel cells (DMFC) (5,524 Wh kg⁻¹) and gasoline engine (11,860 Wh kg⁻¹) than conventional Li-ion batteries. Air cathodes are one of the most challenging subjects in non-aqueous Li-air battery development. One major problem is precipitate of cathode discharge products in non-aqueous electrolytes, which causes voltage loss and eventually shuts down discharge operation.

Lithium compounds Li₂O, Li₂O₂, and Li₂CO₃ are typical discharge products, and extremely low in electric conductivity as indicated by their bandgaps (Li₂O: 7.44 eV, Li₂O₂: 5.12 eV, and Li₂CO₃: 8.83 eV; materials of bandgap > 3 eV are good insulator).² Because of their low solubility in most nonaqueous electrolytes, discharge products precipitate at local reaction sites. Albertus et al. indicated that precipitate exists in thin film that covers the reaction surface, resisting electron transport for electrochemical reactions. Viswanathan et al.³ designed a reversible redox couple to investigate the precipitate's resistance and proposed a metal-insulator-metal charge transport model to predict the electrical conductivity of the precipitate film. Discharge operation was shut down as the film thickness reaches approximately 5 nm to 10 nm. Wang and coworkers indicated that the insoluble product precipitation is similar to ice formation in the fuel cell's cathode during subfreezing operation,⁴⁻⁶ in which ice first nucleates at selected sites, followed by film formation. They elucidated several precipitate growth modes and proposed a coverage model for electrode passivation. Two major mechanisms of voltage loss due to surface coverage and oxygen transport resistance, respectively, were analyzed and compared.^{7,8} Because the precipitates are physically deposited inside the cathode electrode, the electrode structure, including porosity, carbon particle morphology, and tortuosity, greatly influence the voltage loss due to the precipitate accumulation.⁹ Xiao et al.¹⁰ investigated the impacts of carbon microstructure and loading, and found that the cathode capacity increases with the carbon material's mesopore volume. Zhang et al.¹¹ employed galvanostatic discharge, polarization, and AC-impedance techniques, showing that the discharge performance is determined mainly by air cathodes. Mirzaeian and Hall¹² studied the porosity, pore structure, carbon's morphology and surface area of the cathodes, and found that the battery performance is influenced by these parameters. Yang et al.¹³ fabricated bimodal-mesopore cathodes using nanocasting technique, and achieved about 40% capacity increase comparing with commercial carbon black electrodes. Mitchell et al. used hollow carbon fibers of 30 nm diameters in the cathodes,¹⁴ and indicated that Li oxides grew as nodules first and later developed into

toroid. Griffith et al.¹⁵ observed Li oxides form typical 'toroidal' particles at low discharge rates, and exhibit needle-like shapes for high rates, instead of the nano-sheets or compact films. Popular reported morphologies of insoluble precipitates include toroid shape,¹⁶⁻³⁰ film formation,^{2,3,16} and amorphous morphology.^{16,20,23} Studies showed precipitate deposits may reach 1–10 μm in their size.^{9,28,29}

In physical modeling, precipitate's impacts need to be accounted for as one major mechanism of voltage loss. Direct observation of film formation at planar surfaces indicated a film resistor model is suitable to describe associated voltage loss.^{2,4} Wang proposed a surface coverage model for general electrodes including porous cathodes, following the approach in subfreezing operation of PEM fuel cell.^{4,5} In addition, Wang and Cho⁶ indicated that discharge precipitates likely alter the oxygen transport network's tortuosity in the cathode. In this paper, we carried out an experimental study of discharge Li compound precipitate to compare with the model prediction and to investigate the impacts of deposit morphology on model predictions. To exclude the voltage loss associated with oxygen transport and precipitate formation,⁶ Toray carbon cloth, which contains approximately planar reaction surface with large pore's size and volume, was selected as the battery cathode. SEM and XRD were employed to analyze the precipitate's morphology and composite for comparison with model prediction. Both film-resistor model and coverage model were used to predict the discharge voltage behaviors.

Experimental

The experimental Li-air batteries were self-designed to integrate a carbon-cloth cathode and operate with ambient oxygen, see Fig. 1. The cell consists of two aluminum plates as the outer case, two plastic plates as the inner case, and O-ring in the middle to build an enclosure for the anode, membrane separator, and cathode. The upper aluminum and plastic plates have oxygen window in the center, permitting ambient oxygen to diffuse and dissolve into electrolyte. The working components include a Lithium (99.9% trace metals basis, Aldrich) anode, PTFE membrane separator (047022B, MS), and a single piece of carbon cloth (ELAT-H, FuelCellsEtc) as the cathode with an active area of 1 cm × 1 cm. The anode and cathode were placed on a copper wire and Nickel mesh, respectively, which connect to the out-circuit. The electrolyte used DME (anhydrous, 99.5%, Sigma-Aldrich) as the solvent and 1 M Lithium bistrifluoromethanesulfonimide (CF₃SO₂NLiSO₂CF₃, 99.95% trace metals basis, ALDRICH) as conducting salt. DME has been used as an electrolyte for Li-O₂/air battery. It is worth noting that DME has a Gutman acceptor number of about 10 and thus does not induce enough solubility of LiO₂^{*}, i.e. LiO₂^{*} ⇌ Li⁺(sol) + O₂⁻(sol).³¹⁻³³ The cells were assembled in an argon-filled glove box.

*Electrochemical Society Member.

^zE-mail: yunw@uci.edu

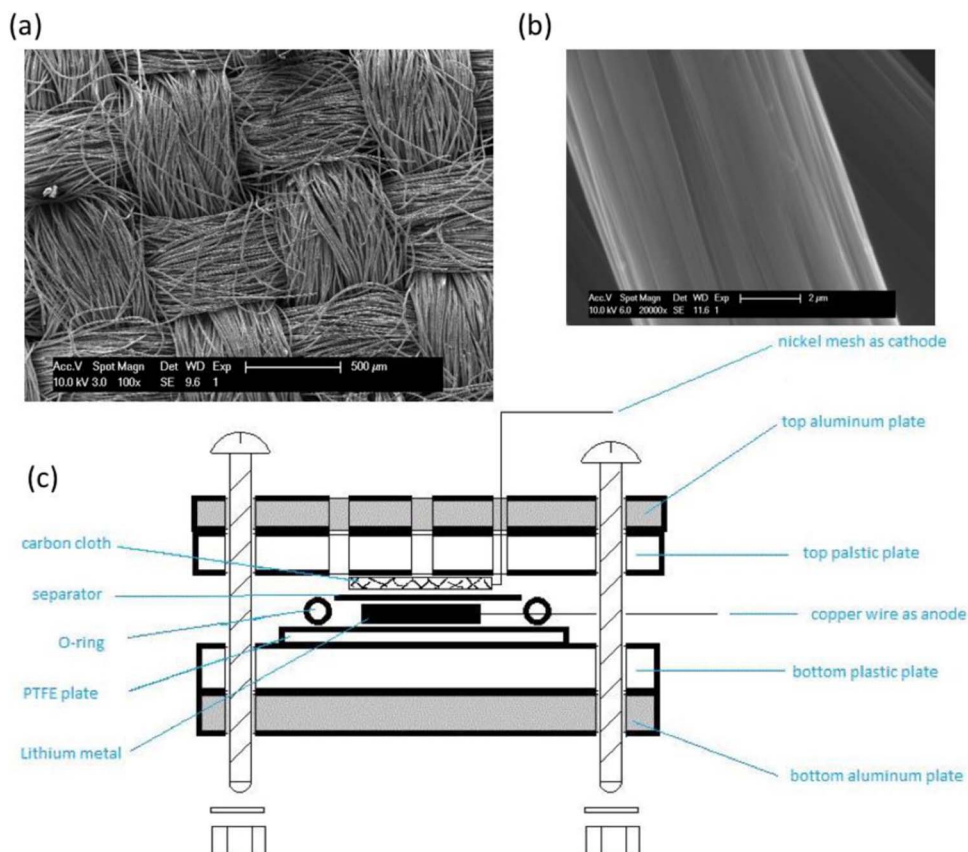


Figure 1. (a) Carbon cloth cathode; (b) Fiber morphology; and (c) Experimental setup for the carbon-cloth Li-air battery.

The cathode solid structure is plain carbon cloth (ELAT-H, Fuel-CellsEtc) and the fibers are woven together without any catalyst and binder, see Fig. 1. It has a thickness around $400\ \mu\text{m}$ and overall density of $13\ \text{mg}/\text{cm}^2$ with a porosity of around 80%, a carbon content of 99.5% in fibers, and a mean pore size around $20\ \mu\text{m}$. The morphology of the constituent fibers can be assumed cylindrical with a diameter around $7\ \mu\text{m}$, see Fig. 1b. The through-plane electrical conductivity is $0.1\ \text{m}\Omega\ \text{cm}^2$. The pore network's tortuosity is about 1.11 through experimental fitting. These material characteristics can be found in Refs. 34,35. Table I documents the physical properties of carbon cloth cathode and experimental parameters.

Battery testing was performed galvanostatically under room temperature using an electrochemical testing platform (Princeton Applied Research, PARSTAT MC, PMC 500/HI). Before measurement, the assembled cell was rested in dry ambient oxygen for at least 120 minutes. Each measurement started with a 30 min recording of the open circuit potential to ensure equilibrium in the cell, followed by applying a constant discharge current. Three current densities were chosen for experiment, including 0.03, 0.06 and $0.10\ \text{mA}/\text{cm}^2$. These current densities are similar to those operated on planar electrodes.² For example, given the specific area of 30 for carbon cloth electrode, the current density of $0.1\ \text{mA}/\text{cm}^2$ in the present study is equivalent to $\sim 3.33\ \mu\text{A}/\text{cm}^2$ for a planar electrode, which is similar to that of $3.76\ \mu\text{A}/\text{cm}^2$ in the study.² Discharge products were characterized by the Rigaku SmartLab X-ray Diffractometer (Cu-K β source, 40 kV, 44 mA) and SEM (Philips XL-30 FEG SEM). All the SEM images were taken at the side of cathode near the current collector.

Modeling Voltage Loss due to Precipitates

Film-resistor model.—Assuming the precipitates form thin film covering the reaction surface, the film becomes a resistor hampering

Table I. Experimental and modeling parameters.

Experimental Parameter	Value/description
The active area of Li-air battery	$1 \times 1\ \text{cm}^2$
PTFE membrane separator/cathode thickness	$150/406\ \mu\text{m}$
Electrolyte	DME+1M $\text{CF}_3\text{SO}_2\text{NLiSO}_2\text{CF}_3$
Fiber radius of cathode, r_f ³⁵	$3.5\ \mu\text{m}$
Cathode mean pore size ³⁵	$\sim 20\ \mu\text{m}$
Cathode porosity, ϵ_0 ³⁴	0.8
Cathode tortuosity ³⁵	1.11
Cathode through-plane conductivity ³⁴	$0.1\ \text{m}\Omega\ \text{cm}^2$
Current density I	0.03, 0.06 and $0.1\ \text{mA}/\text{cm}^2$
Operating temperature	25°C
Operating pressure	1 atm
Model Parameter	
The specific area ratio, A^*	30
Oxygen diffusivity and solubility in electrolyte ⁴	$4 \times 10^{-5}\ \text{cm}^2/\text{s}$ and 0.00876 in DME with of 1 M Li^+
Discharge product (Li_2CO_3) molecular weight, M_{prod}	$0.07389\ \text{kg}/\text{mol}$
Discharge product (Li_2CO_3) density, ρ_{prod}	$2,110\ \text{kg}/\text{m}^3$
A_0 in the film-resistor model ⁴	$1.0 \times 10^{15}\ \Omega\ \text{m}$
c_1 and c_2 in the film-resistor model ^{2,4}	$4.7 \times 10^7\ \text{m}^{-1}$ and $3.6 \times 10^{-7}\ \text{m}$
B_1 , B_2 , and s_0 in the coverage model ^{4,6,7}	2.5, 8, and 0.2
$\epsilon_{\text{prod,max}}$ in the coverage model	0.0035, 0.009, and 0.0425 for 0.1, 0.06, and $0.03\ \text{A}/\text{cm}^2$, respectively

*Estimate.

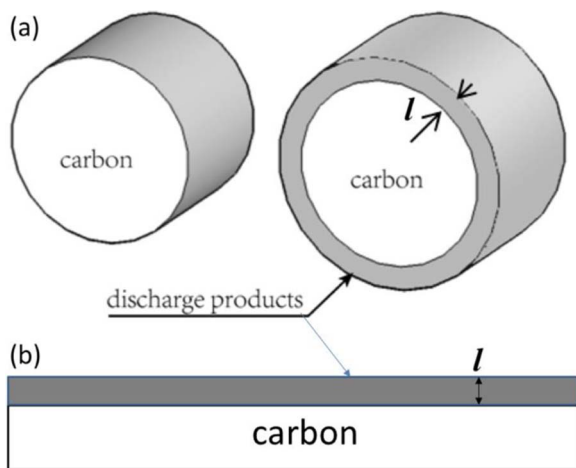


Figure 2. Thin film growth mode of precipitates on: 1.) cylindrical fiber and dimension; and 2.) planar surface.⁴

electron transport and causing voltage loss,²⁻⁴ see Fig. 2. The precipitate film grows usually around 10–100 nm in thickness before shutting down discharge operation. For the carbon cloth cathode, the film grows at the cylindrical surface of fibers with its thickness l given by:⁴

$$l = \left(1 - \sqrt{\frac{\epsilon_f + \epsilon_{prod}}{\epsilon_f}} \right) r_f \quad [1]$$

As the discharge operation proceeds, both the volume fraction of discharge product ϵ_{prod} and film thickness l increase, raising the reaction resistance and voltage loss. The method of formulating film thickness was employed for a spherical reaction surface.² For the carbon cloth cathode, its fiber radius r_f is around 3.5 μm ($\gg l$), thus the deposit film can be approximated by the planar-film growth mode,⁴ in which the film thickness is directly determined by the discharge product volume:

$$Al = \frac{QM_{prod}}{nF\rho_{prod}} \quad [2]$$

where A denotes the specific area ratio. The coulomb of discharge Q per active reaction area (mA h/cm^2) is given by:

$$Q = \int_0^t Idt \xrightarrow{I=\text{constant}} Q = I \times t \quad [3]$$

The above equation assumes that the film were firmly packed without any pores and all the discharge products were precipitated in the film. The electric resistance R_{prod} is determined by the thickness l , empirically given by:^{2,4}

$$R_{prod} = A_0 l \exp [c_1 (l - c_2)] \quad [4]$$

where c_1 and c_2 are constant. The voltage loss associated with the film formation is then given by:

$$\Delta\eta = -i_n R_{prod} = -\frac{I}{A} R_{prod} \quad [5]$$

where I represents the average current density and i_n denotes the current density across the discharge film in the direction normal to the reaction surface. The film-resistor model was compared with experimental data and showed acceptable agreement.^{2,4}

Surface coverage model.—The resistance of electron access to electrochemical reaction caused by insoluble discharge products can be evaluated through reduction in the active reaction surface area, a . For porous electrodes, the following power law is frequently adopted

to describe the reduced surface area:^{4,35}

$$a = a_0(1 - s)^{\tau_a} \quad \text{where} \quad s = \frac{\epsilon_{prod}}{\epsilon} \quad [6]$$

where s represents the volume fraction of insoluble discharge products in the pore space, and τ_a is the exponent coefficient that measures the degree of insoluble products' effect on the active surface area. The below semi-empirical relationships were proposed to describe the coverage coefficient:^{4,6,7}

$$\tau_a = \begin{cases} B_1 \frac{l}{l_0} & s < s_0 \\ \frac{l}{l_0} (B_1 + B_2(s - s_0)) & \text{otherwise} \end{cases} \quad [7]$$

In the above equation, the maximum value of s is assumed to be unity, i.e. the precipitates occupy the entire pore space. In the present study, the porosity and pore size are large, and the reaction surface area is small. As a result, the maximum of s is much smaller than 100%. We then modify the reduced surface area and the coverage coefficient in the above two equations by defining the volume fraction of insoluble discharge product, s , as below (instead of that in Eq. 6):

$$s = \frac{\epsilon_{prod}}{\epsilon_{prod,max}} \quad [8]$$

where $\epsilon_{prod,max}$ represents the maximum volume fraction that discharge product may occupy under the operating condition. It is determined by multi-factors including the number of activation sites, surface area, and discharge product morphology. In design of high energy density battery, it is desirable that $\epsilon_{prod,max}$ is close to porosity ϵ .

As discharge proceeds, precipitate accumulates, narrowing the pore network and thus increasing oxygen transport resistance and associated voltage loss. In the present cathode, this voltage loss is anticipated to be unimportant, which can be justified by evaluating the Damköhler number (Da):⁹

$$Da = \frac{I}{8F} \frac{\delta}{C_{O_2,\delta} D_{O_2} \epsilon_0^{\tau_{d,0}}} = \frac{\text{Reaction rate}}{\text{Mass transport rate}} \quad [9]$$

A current density of 0.1 mA/cm^2 or 1 A/m^2 , δ of 0.4 mm, ϵ_0 of 0.8, $\tau_{d,0}$ of 1.1, and D_{O_2} of 4×10^{-9} m^2/s yield $Da \sim 0.03$ for $C_{O_2,\delta}$ of 5 mol/m^3 (5 mM), clearly indicative of sufficiently fast mass diffusion relative to the reaction kinetics under the discharging current. Even precipitate occupies 75% of the pore space, i.e. the effective porosity becomes 0.2, Da is around 0.14 under the same tortuosity, indicating oxygen supply is sufficient for the reaction. For the lowest current in this experiment, i.e. 0.03 mA/cm^2 , Da is around 0.042 for a porosity of 0.2.

To evaluate the voltage loss due to oxygen transport and precipitates, one can adopt the below formula⁷ to assess the surface overpotential at the middle depth of the cathode:

$$\Delta\eta_{O_2} \left(y = \frac{\delta}{2} \right) = \frac{RT}{F} \ln \left(1 - \frac{3Da}{4\epsilon^{\tau_d - \tau_{d,0}} \left(1 - \frac{\epsilon_{prod}}{\epsilon} \right)^{\tau_d}} \right) \quad [10]$$

An approximate model can then be developed by combining the two voltage losses raised by the surface coverage and oxygen transport when precipitates are present:⁷

$$\begin{aligned} \Delta\eta &= \frac{RT}{(1 - \beta)F} \left(\tau_a \ln(1 - s) \right. \\ &\quad \left. + (1 - \beta) \ln \left(1 - \frac{3Da}{4\epsilon^{\tau_d - \tau_{d,0}} \left(1 - \frac{\epsilon_{prod}}{\epsilon} \right)^{\tau_d}} \right) \right) \\ &= \Delta\eta_a + \Delta\eta_{O_2} \end{aligned} \quad [11]$$

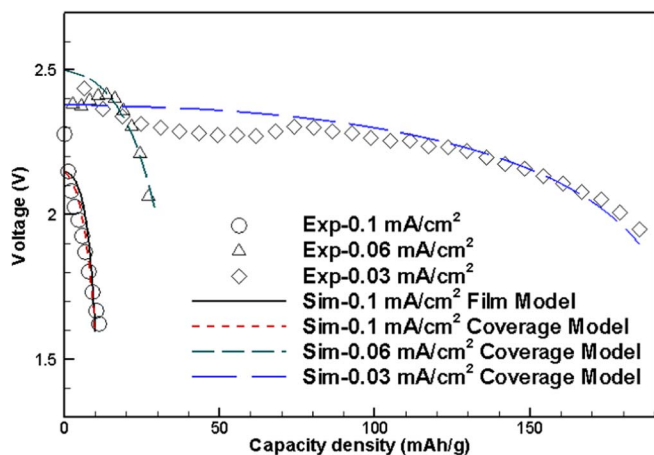


Figure 3. Discharge voltage evolution of Li-air battery and comparison with model predictions. The film-resistor model's prediction considerably deviates from the experimental data under the two low currents, which is not plotted in the figure.

where $\Delta\eta_a$ and $\Delta\eta_{O_2}$ represent the voltage losses associated with precipitates due to surface coverage and oxygen transport, respectively.

Results and Discussion

Fig. 3 plots the experimental discharging voltage evolution under 0.03, 0.06, and 0.1 mA/cm², along with model prediction. The battery output voltage experienced a decreasing trend in general as discharging proceeds, which is typical as observed by other studies.^{2,4,36} In the model prediction, the film-resistor model adopted the parameters similar to Albertus et al.² and Wang,⁴ and the coverage model used the same parameters as Wang and coworkers.^{6,7,9} The coverage model prediction shows acceptable agreement with all the experimental data. The voltage loss due to oxygen transport associated with precipitates $\Delta\eta_{O_2}$ is plotted in Fig. 4, showing that its contribution is small relative to the overall voltage loss and thus is negligible, which is consistent with the Da analysis in Eq. 9. In addition, the film-resistor model predicts the voltage loss under the highest current density (0.1 mA/cm²) but fails to match with the other two lower current operations (significantly under-predicts the battery capacities). To explore the reasons for the observed deviation, both SEM and XRD were carried out to disclose the morphology and composition of deposits in the cathode electrodes.

In the imaging, the carbon-cloth cathode was taken out at the end of the discharging operation, gently washed by fresh solvent, and dried in

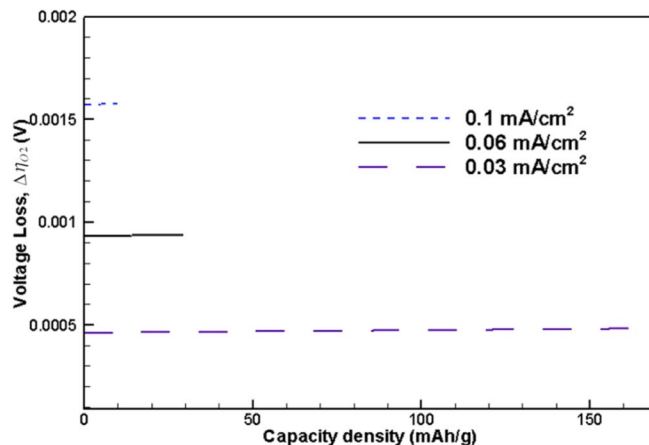


Figure 4. Predicted $\Delta\eta_{O_2}$ in Eq. 11 for the three current densities.

a sealed space. The samples were then imaged using SEM, as shown in Fig. 5a for 0.03 mA/cm². XRD was performed after the SEM imaging, as shown in Figure 5b, and indicated that the white deposit is primarily Li₂CO₃. Some studies indicated that electrolyte decomposition may result in Li₂CO₃ formation.^{2,37} It is also possible that the direct discharge products in the battery are lithium oxides, which then react with ambient CO₂ to form Li₂CO₃ during testing or imaging. Because both Li oxides and Li₂CO₃ are intrinsic insulator with extremely low conductance to electron transport,^{2,38} their formation at the reaction surface hampers electron transport for the electrochemical reaction, leading to passivation.

Three morphologies of discharge precipitates are evident in Fig. 5a: 1) film formation over the fiber's cylindrical surface, see Fig. 6; 2.) large aggregates (at the scale of about/over 10 μm in size) attaching to fibers, see Fig. 7; and 3.) small aggregates (at the scale of 1 μm in size), see Fig. 8. It is clear that the majority of the pore space in the cathode is not clogged by the precipitate and most pores remain open for reactant transport via electrolyte. The precipitate occupied a small fraction of the void space, thus the voltage loss due to the oxygen transport resistance raised by the precipitate formation is unimportant, as shown in the preceding analysis on the Da number and Fig. 4. In Fig. 6, a thin film clearly develops at the carbon fiber surface, which introduces a barrier to electron transport and yields a voltage drop in the operation. Electron tunneling is one possible mechanism enabling electrons to across the thin insulation layer for the electrochemical reaction.³ The thin film usually grows about tens of nanometers in thickness depending on operation condition. Similar film formation

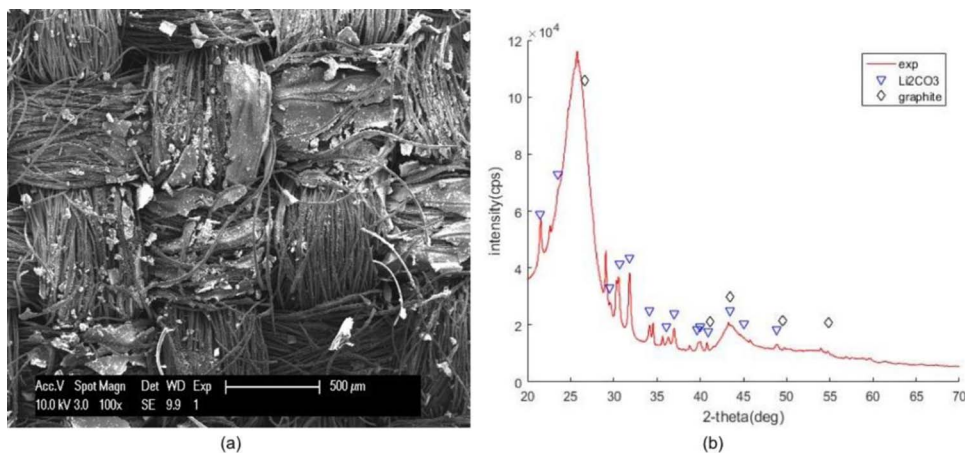


Figure 5. SEM images and XRD analysis of the cathode with discharge precipitate under 0.03 mA/cm².

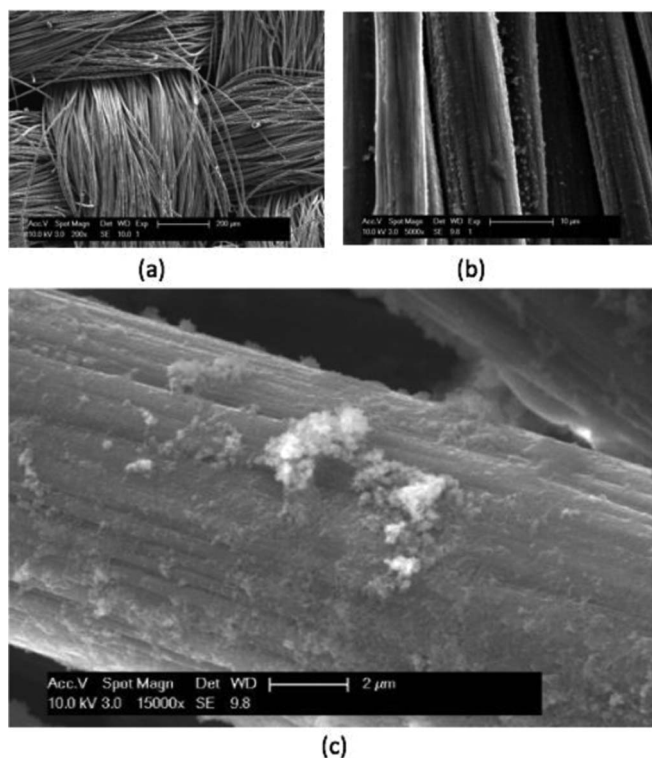


Figure 6. Film formation of discharge precipitate under 0.03 mA/cm^2 .

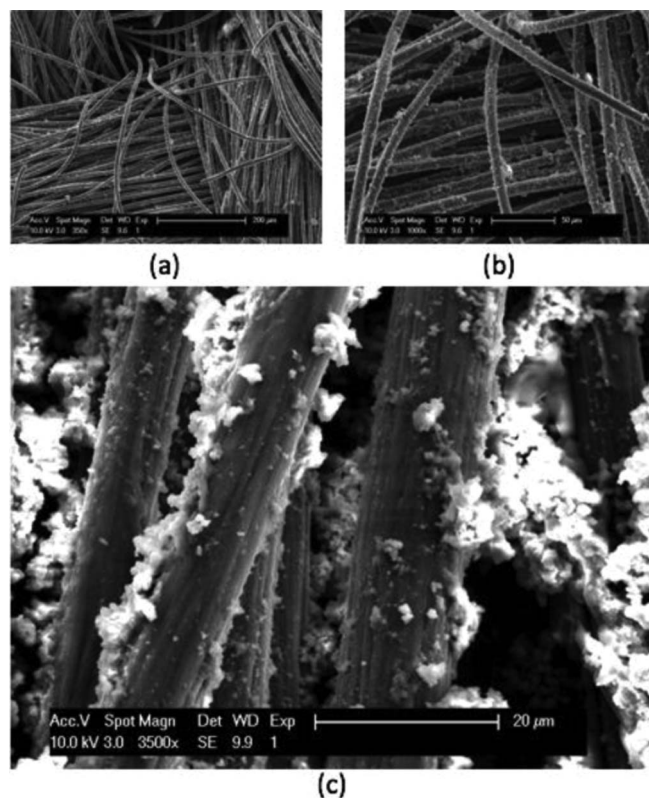


Figure 8. Small aggregate formation of discharge precipitate under 0.03 mA/cm^2 .

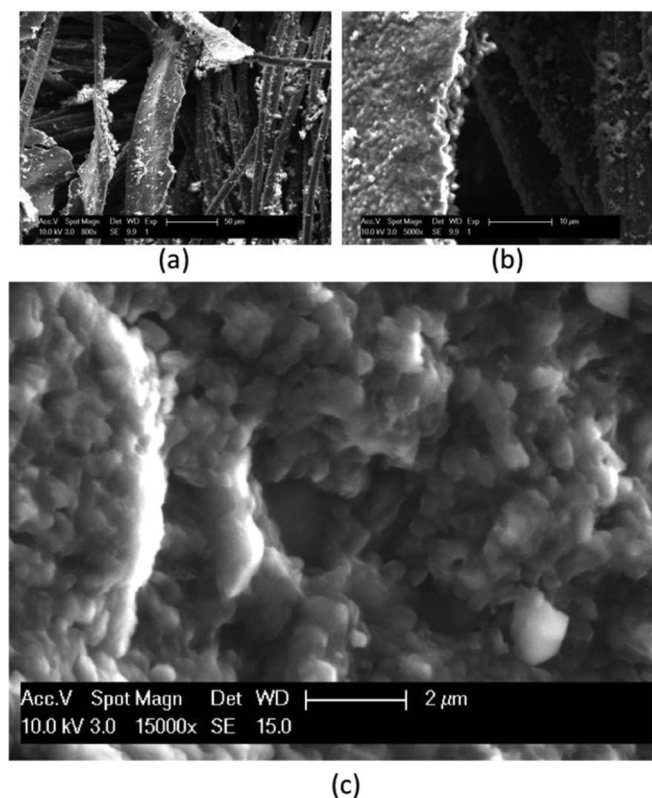


Figure 7. Large aggregate formation of discharge precipitate under 0.03 mA/cm^2 .

was observed by Albertus et al.,² Viswanathan et al.,³ Black et al.,¹⁶ Yang et al.,²⁸ and Yu et al.³⁹

Fig. 7 shows formation of large precipitate aggregates which are present near the air side of the cathode. The agglomerates grow around fibers with their size even beyond $10 \mu\text{m}$. It is seen that the aggregates consist of many small particles of a dimension around $200\text{--}500 \text{ nm}$ with grain boundaries. It is difficult to see the morphology of all the small particles, but some exhibit the spherical or toroidal shape. The actual mechanism is unclear for the observed aggregation of the dimension. It is possibly due to the presence of grain boundaries which permit the reactant transport for the electrochemical reaction. The aggregates appear to cover a small area of the cathode, which raise oxygen transport resistance only at local for the present cathode. However, aggregates of the dimension may effectively block oxygen transport in cathodes of small pores, raising voltage loss. Yang et al.,²⁸ Zhai et al.²⁹ and Wang et al.⁹ observed discharge deposits of similar dimension in their studies.

In several locations of cathode, the white discharge deposit exists in relatively small aggregates at a scale of approximately $1 \mu\text{m}$ in size, distributed randomly on the fiber surface, as shown in Fig. 8. Similarly, the aggregates appear to consist of small particles with a dimension around $200\text{--}500 \text{ nm}$. Different with the large aggregates, these aggregates are small and unable to surround the fiber perimeter. Similar morphology was observed by Adams et al.,²⁶ Xia et al.²⁷ and Johnson et al.⁴⁰ Their presence appears to have little impacts on oxygen diffusion for the present cathode; but could be significant for cathode pores at nano- or mesoscale.

For the above two morphologies of deposit aggregates, their impacts on voltage loss are not fully understood yet. It is clear that their impacts deviate from the film resistor approach which assumes the precipitate form a thin film — a resistive layer hampering electron transport. This may be the major reason that the film-resistor model prediction failed to match with the experimental data for 0.03 mA/cm^2 in Fig. 3. As to the coverage model, the precipitates' impact

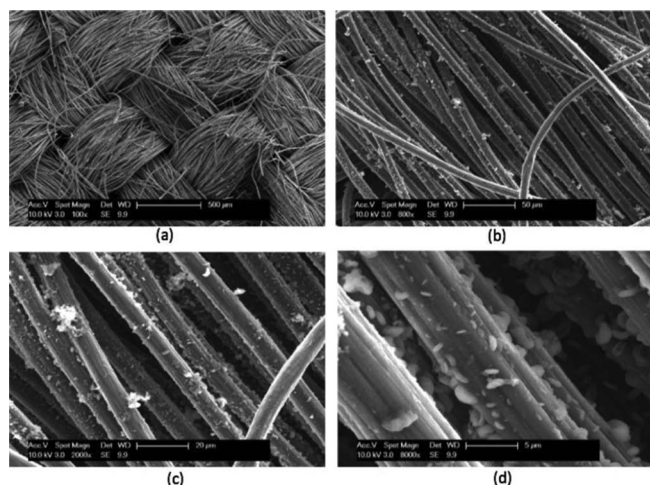


Figure 9. Film and toroid formation of discharge precipitate under 0.06 mA/cm².

is converted to loss of the electrochemical reaction area, following the approach of the ice's effect on PEM fuel cell's voltage loss.⁴ The precipitates, in either film or aggregate form, covers certain area of fibers and reaction sites, reducing the electrochemical activity. Therefore, the coverage model shows acceptable match with the experimental data. In addition, it appears that the presence of these aggregates may increase the storage capacity of Li discharge deposit and hence battery capacity. Their presence will affect bulk oxygen transport inside micro- or nano-scale pores. In addition, water or organic carbonates were found to significantly affect the performance of Li-O₂ batteries using Vulcan-based positive electrodes.⁴¹ It is likely these additive species would impact the morphology of discharge deposit as well,³¹ yielding various deposit shape/size. Similarly, it would be difficult for the film-resistor model to account for various deposit morphology and hence the impacts of the additives.

Fig. 9 displays the precipitate of discharge products under 0.06 mA/cm², showing that both thin film and toroidal (or partially toroidal) precipitates are present at the fiber surface. The toroidal deposits are small around 1 µm in size. Similar morphology was observed by Refs. 16–30. The amount of the toroidal deposit appears much smaller than the pore space, thus its effect on the oxygen transport polarization is negligible. Similarly, this morphology's impact on electrode passivation deviates from the film-resistor model, which explains the mismatch with the experimental data in Fig. 3. The toroidal deposits on the fiber surface covers the reaction surface and reduces the electrochemical activity, which is accounted by the coverage model. Thus, the coverage model predicts the experimentally observed voltage loss.

Fig. 10 presents the precipitate under 0.1 mA/cm², showing that film formation dominates the morphology of the precipitate. The film appears very thin, tightly covering the fiber surface. The film resists electron transport for the electrochemical reaction, causing electrode passivation. The film-resistor model describes this type of deposit

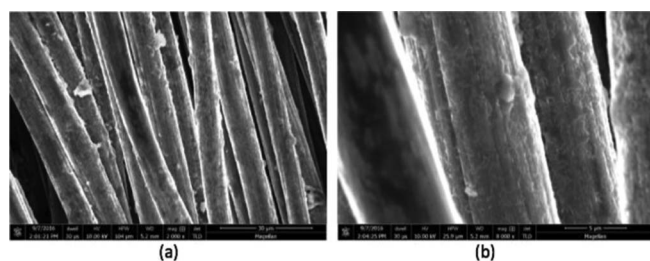


Figure 10. Film formation of discharge precipitate under 0.1 mA/cm².

morphology, and thus predicts the voltage evolution under this current. The maximum thickness of the thin film is predicted to be around 40 nm from the model prediction, which is in line with the work of Albertus et al.² and Wang⁴ (~40 nm under the current of 3.76 µA/cm² on a planar electrode;² in the present work, the current of 0.1 mA/cm² is converted to ~3.33 µA/cm² equivalent current for a planar surface). In addition, the deposit film's thickness is consistent with Luntz et al.,⁴² which adopted the same film-resistor model (In the Fig. 2b of Luntz et al.,⁴² the film thickness is about 8 nm at 20°C and much larger than 9 nm at 40°C under the current of 3.0 µA/cm². The present work reports about 40 nm thickness under 25°C and ~3.33 µA/cm² equivalent current.) For the surface coverage model, the thin-film formation imposes a surface coverage on the electrochemical reaction sites, reducing the electrochemical reactivity. Thus, the impact of this growth mode of precipitates was captured by the coverage model as well. Similar conclusion was drawn by Wang.⁴ In addition, the discussion can be extended to the cases where Li₂O₂ is the primary product. Because various morphology of Li₂O₂ deposit was observed as well, a single-morphology model, i.e. the film-resistor model, cannot account for the impact of deposit morphology other than film formation. The surface coverage model may be more accurate in predicting the impact of various morphology and voltage loss.

Conclusions

In this work, we compared the predictions of two Li-air battery models, namely the film-resistor model and surface coverage model, with experimental data to study the discharge voltage loss and the precipitate morphology's impacts on model prediction. Acceptable agreement was achieved for the coverage model, while the film-resistor model failed to match with the experimental data for the two low current densities, i.e. 0.03 and 0.06 mA/cm². SEM and XRD were employed to explore the observed discrepancy. Several morphologies of discharge deposit were disclosed for the two lower currents, including film formation, large aggregates, small aggregates, and toroidal shapes. The aggregate precipitates were found to be present at a length scale of micrometer and to consist of small nanoparticles around 200–500 nm. Presence of grain boundaries was a possible mechanism for observed aggregation. The impacts of the aggregate and toroidal morphologies on voltage loss deviated from that of film formation, and were attributed as the major reason that the film-resistor model prediction failed to match with the experimental data. For the highest current 0.1 mA/cm², thin film formation dominated and the film-resistor model prediction agreed well with the experimental data using the model parameters reported in the literature. The coverage model predicted the experimental data for all the cases because the model accounts for the effects of various deposit morphologies on the electrochemical activity. In addition, it indicated that the voltage loss associated oxygen transport and precipitates was small and negligible in the cases of study.

Acknowledgment

We gratefully acknowledge the support of the National Science Foundation (CBET-1336873) on this study.

References

- P. G. Bruce, S. A. Frauberger, L. J. Hardwick, and J.-M. Tarascon, "Li-O₂ and Li-S batteries with high energy storage," *Nat. Mater.*, **11**, 19 (2012).
- P. Albertus, G. Girishkumar, B. McCloskey, R. S. Sánchez-Carrera, B. Kozinsky, J. Christensen, and A. C. Luntz, "Identifying capacity limitations in the Li/oxygen battery using experiments and modeling," *Journal of the Electrochemical Society*, **158**, A343 (2011).
- V. Viswanathan, K. S. Thygesen, J. S. Hummelshøj, J. K. Nørskov, G. Girishkumar, B. D. McCloskey, and A. C. Luntz, "Electrical conductivity in Li₂O₂ and its role in determining capacity limitations in non-aqueous Li-O₂ batteries," *J. Chem. Phys.*, **135**, 214704 (2011).
- Y. Wang, "Modeling discharge deposit formation and its effect on lithium-air battery performance," *Electrochimica Acta*, **75**, 239 (2012).

5. J. Mishler, Y. Wang, P. P. Mukherjee, R. Mukundan, and R. L. Borup, "Subfreezing operation of polymer electrolyte fuel cells: Ice formation and cell performance loss," *Electrochimica Acta*, **65**, 127 (2012).
6. Y. Wang and S. C. Cho, "Analysis and Multi-Dimensional Modeling of Lithium-Air Batteries," *Journal of the Electrochemical Society*, **162**, A114 (2015).
7. Y. Wang and S. C. Cho, "Analysis of air cathode performance for lithium-air batteries," *J. Electrochem. Soc.*, **160**, A1847 (2013).
8. Y. Wang, "analysis of the key parameters in the cold start of polymer electrolyte fuel cells," *J. Electrochem. Soc.*, **154**, B1041 (2007).
9. Y. Wang, Z. Wang, H. Yuan, and T. Li, "Discharge oxide storage capacity and voltage loss in Li-air battery," *Electrochimica Acta*, **180**, 382 (2015).
10. J. Xiao, D. Wang, W. Xu, R. E. Williford, J. Liu, and J. Zhang, "Optimization of air electrode for Li/air batteries," *J. Electrochem. Soc.*, **157**, A487 (2010).
11. S. S. Zhang, D. Foster, and J. Read, "Discharge characteristic of a non-aqueous electrolyte Li/O₂ battery," *J. Power Sources*, **195**, 1235 (2010).
12. M. Mirzaeian and P. J. Hall, "Preparation of controlled porosity carbon aerogels for energy storage in rechargeable lithium oxygen batteries," *Electrochim. Acta*, **54**, 7444 (2009).
13. X. Yang, P. He, and Y. Xia, "Preparation of mesocellular carbon foam and its application for lithium/oxygen battery," *Electrochem. Comm.*, **11**, 1127 (2009).
14. R. R. Mitchell, B. M. Gallant, C. V. Thompson, and S. H. Yang, "All-carbon-nanofiber electrodes for high-energy rechargeable Li-O₂ Batteries," *Energy Environ. Sci.*, **4**, 2952 (2011).
15. L. D. Griffith, A. Sleightholme, J. F. Mansfield, D. J. Siegel, and C. W. Monroe, "Correlating Li/O₂ cell capacity and product morphology with discharge current," *ACS Appl. Mater. Interfaces*, **7**, 7670 (2015).
16. R. Black, S. H. Oh, J.-H. Lee, T. Yim, B. Adams, and L. F. Nazar, *J. Am. Chem. Soc.*, **134**, 2902 (2012).
17. R. R. Mitchell, B. M. Gallant, C. V. Thompson, and Y. Shao-Horn, *Energy Environ. Sci.*, **4**, 2952 (2011).
18. Z.-L. Wang, D. Xu, J.-J. Xu, L.-L. Zhang, and X.-B. Zhang, *Adv. Funct. Mater.*, **22**, 3699 (2012).
19. Y.-C. Lu, D. G. Kwabi, K. P. C. Yao, J. R. Harding, J. Zhou, L. Zuin, and Y. Shao-Horn, *Energy Environ. Sci.*, **4**, 2999 (2011).
20. W. Fan, Z. Cui, and X. Guo, *J. Phys. Chem. C*, **117**, 2623 (2013).
21. R. R. Mitchell, B. M. Gallant, Y. Shao-Horn, and C. V. Thompson, *J. Phys. Chem. Lett.*, **4**, 1060 (2013).
22. B. Horstmann, B. Gallant, R. Mitchell, W. G. Bessler, Y. Shao-Horn, and M. Z. Bazant, *J. Phys. Chem. Lett.*, **4**, 4217 (2013).
23. E. Yilmaz, C. Yogi, K. Yamanaka, T. Ohta, and H. R. Byon, *Nano Lett.*, **13**, 4679 (2013).
24. L. Zhong, R. R. Mitchell, Y. Liu, B. M. Gallant, C. V. Thompson, J. Y. Huang, S. X. Mao, and Y. Shao-Horn, *Nano Lett.*, **13**, 2209 (2013).
25. B. M. Gallant, D. G. Kwabi, R. R. Mitchell, J. Zhou, C. V. Thompson, and Y. Shao-Horn, *Energy Environ. Sci.*, **6**, 2518 (2013).
26. B. D. Adams, C. Radtke, R. Black, M. L. Trudeau, K. Zaghbi, and L. F. Nazar, *Energy Environ. Sci.*, **6**, 1772 (2013).
27. C. Xia, M. Waletzko, L. Chen, K. Peppler, P. J. Klar, and J. Janek, *ACS Appl. Mater. Interfaces*, **6**, 12083 (2014).
28. Y. Yang, W. Liu, Y. Wang, X. Wang, L. Xiao, J. Lu, and L. Zhuang, *Phys. Chem. Chem. Phys.*, **16**, 20618 (2014).
29. D. Zhai, H.-H. Wang, K. C. Lau, J. Gao, P. C. Redfern, F. Kang, B. Li, E. Indacochea, U. Das, H.-H. Sun, H.-J. Sun, K. Amine, and L. A. Curtiss, *J. Phys. Chem. Lett.*, **5**, 2705 (2014).
30. D. Zhai, H.-H. Wang, J. Yang, K. C. Lau, K. Li, K. Amine, and L. A. Curtiss, *J. Am. Chem. Soc.*, **135**, 15364 (2013).
31. N. B. Aetukuri, B. D. McCloskey, J. M. Garcia, L. E. Krupp, V. Viswanathan, and A. C. Luntz, *Nature Chemistry*, **7**(1), 50.
32. C. M. Burke, V. Pande, A. Khetan, V. Viswanathan, and B. D. McCloskey, *Proc. Natl. Acad. Sci. U S A*, **112**, 9293.
33. I. Gunasekara, S. Mukerjee, E. J. Plichta, M. A. Hendrickson, and K. M. Abraham, *J. Electrochem. Soc.*, **162**(6), A1055 (2015).
34. ELAT Gas Diffusion Layers and ELAT Hydrophilic, <http://fuelcellsetc.com/store/DS/ELAT-Property-Sheet.pdf>.
35. Y. Wang, K. S. Chen, and S. C. Cho, *PEM Fuel Cells: Thermal and Water Management Fundamentals (Sustainable Energy)*, Momentum Press (2013).
36. S. S. Zhang and J. Read, "Partially fluorinated solvent as a co-solvent for the non-aqueous electrolyte of Li/air battery," *J. Power Sources*, **196**, 2867 (2011).
37. J. L. Shui, H. H. Wang, D. J. Liu, and "Degradation and revival of Li-O₂ battery cathode," *Electrochemistry Communications*, **34**, 45 (2013).
38. B. D. McCloskey, A. Speidel, R. Scheffler, D. C. Miller, V. Viswanathan, J. S. Hummelshøj, J. K. Nørskov, and A. C. Luntz, *The Journal of Physical Chemistry Letters*, **3**(8), 997.
39. Y. Yu, B. Zhang, Y.-B. He, Z.-D. Huang, S.-W. Oh, and J.-K. Kim, *J. Mater. Chem. A*, **1**, 1163 (2013).
40. L. Johnson, C. Li, Z. Liu, Y. Chen, S. A. Freunberger, P. C. Ashok, B. B. Praveen, K. Dholakia, J.-M. Tarascon, and P. G. Bruce, *Nature Chemistry*, **6**, 1091 (2014).
41. S. Meini, M. Piana, N. Tsiouvaras, A. Garsuch, and H. A. Gasteiger, *Electrochem. Solid-State Lett.*, **15**(4), A45 (2012).
42. A. C. Luntz, V. Viswanathan, J. Voss, J. B. Varley, J. K. Nørskov, R. Scheffler, and A. Speidel, *The Journal of Physical Chemistry Letters*, **4**, 3494.